CrossMark

Simulative aurintricarboxylic acid molecular docking with antitumor activity for its VO(II), Cr(III), Mn(II) and Fe(III) complexes, HF/DFT modeling and elaborated EPR studies

F. A. Saad[1] · M. G. Elghalban[1,2] · Jabir H. Al-Fahemi[1] · N. Yarkandy[1] ·
Nashwa M. El-Metwaly[1,2] · K. S. Abou-Melha[3] · G. A. Al-Hazmi[3,4] ·
K. A. Saleh[5]

Abstract A synthesized aurintricarboxylic acid (ATA) complex was deliberately investigated. Spectral, thermal, theoretical and antitumor studies are accomplished in this study. Elaborated electronic and EPR considerations are introducing parameters support the structural discussion of complexes. Octahedral geometry is proposed for all complexes except VO(II) is a square-pyramidal configuration. Molecular modeling utilizing Gaussian 09 program (HF/DFT) was used to verify the mode of bonding through the optimized geometries as well as essential quantum parameters were calculated using frontier energies (E_{HOMO} & E_{LUMO}). The soft character of the complexes may expect their excellent biological feature. The molecular docking computational achievement displays distinguished bounds of ATA drug with human colorectal carcinoma and human hepatic carcinoma. However, the interaction with human breast carcinoma receptor is completely absent. This behavior may clarify the antitumor activity of the complexes under investigation. The experimental work was supported with docking for carcinoma receptors used experimentally. VO(II) complex displays distinguished inhibition activity toward human carcinoma used. This is pointed to the other important use for ATA drug complexes exceeding the antibacterial field.

Keywords Schiff base · HF/DFT · Molecular docking · Antitumor and EPR

✉ Nashwa M. El-Metwaly
n_elmetwaly00@yahoo.com

[1] Chemistry Department, College of Applied Sciences, Umm Al-Qura University, Makkah, Saudi Arabia

[2] Chemistry Department, Faculty of Science, Mansoura University, Mansoura, Egypt

[3] Chemistry Department, Faculty of Science, King Khalid University, P.O. Box 9004, Abha, Saudi Arabia

[4] Chemistry Department, Faculty of Applied Sciences, Taiz University, P.O. Box 82, Taiz, Yemen

[5] Biology Department, Faculty of Science, King Khalid University, P.O. Box 9004, Abha, Saudi Arabia

Introduction

Aurintricarboxylic acid (ATA) is a polymeric carboxylated triphenylmethane derivative [1] with versatile biological activities and modes of actions. Enzymatic inhibitory effects due to binding toward nucleic acid, DNA and RNA polymerases, nucleases, DNA topoisomerase and reverse transcriptase (RT) were included [2]. In addition, ATA has also been reported to inhibit protein synthesis by blocking RNA association with ribosomes disrupt cellular signaling pathways by diverse mechanisms. Also, reinforcement of cell existence in response to assortment suffers in distinct cell types [3]. Progresses in bio-coordination chemistry are very important to improve drug design and to reduce the undesirable side effects, frequently associated with coordinating metals. Cr(III) and Mn(II) complexes for ATA were previously prepared and investigated. The isolated complexes were 1:2 (L/M) molar ratio [2, 4]. Manganese in coordination field entices much interest due to its considerable magnitude in various biological systems [5–8]. Biological activities of some Fe(III) complexes were investigated for 1:2 molar ratio (metal/ligand) [9]. Substationally, inert and stable metal complexes are observed with chromium(III) ion. Chromium(III) complexes are

significantly lower in cytotoxic than chromium(VI) to cultured human cells. In living organisms, vanadium complexes play a significant role in catalytic organic chemistry [10]. Tracey and Thompson have been reported vanadium complexes [11, 12] showing insulin-mimetic activity in vitro studies and displaying positive treatment effects on animals and subjects with diabetes mellitus. Antitumor and antileukemic agents were abstracted from vanadium complexes with definite amino acids [13, 14]. In this study, we focus on synthesis of new metal ion complexes derived from aurintricarboxylic acid drug. Choice of metal ions has a broad history in biological field. Elaborated spectral studies especially EPR are used to verify structural geometries. Computational studies are also under interest, molecular modeling and docking, to assist on optimized geometries and interaction behavior of the acid toward different human carcinoma. Antitumor activity is the major goal in our study to orient the use of antibacterial drug onto another side of diseases.

Experimental

Reagents

The used compounds are commercially available from Sigma-Aldrich. Aurintricarboxylic acid drug (ATA) and sulpho-rhodamine B(SRB) were utilized as it is. The metal salts $MnCl_2 \cdot H_2O$, $Fe(NO_3)_3 \cdot 9H_2O$, $Cr(NO_3)_3 \cdot 9H_2O$ and $VOSO_4 \cdot XH_2O$ are concerned in this study to abstract the metal ion complexes. The solvents used (methanol, ethanol, DMSO, triethylamine) are implemented without previous purification. Culture media and growth supplements were purchased from Gibco/Life Technologies Co, (Carlsbad, CA, USA). Cell culture vessels were purchased from Nunc Co. (Roskilde, Denmark). Colorectal carcinoma (HCT-116), hepatic carcinoma (HEPG-2) and breast carcinoma (MCF-7) were taken from Vacsera (Giza, Egypt).

Preparation process of metal ion complexes

The metal ion complexes were synthesized. Synthesis of all complexes were carried out by the same approach except Cr(III) complex. The precipitation of its complex needs few drops of triethylamine to accelerate the complexation process. Cr(III) or Mn(II)-ATA complexes were previously reported [2, 4], and the isolated complexes are significantly different from that prepared in our study. 1:2 molar ratio (L/M) is the general ratio used in this study to give a chance for poly nuclear complexes with high yields. 0.422 g of (1 mmol) ATA drug (red color) was added drop-wisely to each metal salt as; 0.3258 g anhydrous $VOSO_4$, 0.8004 g $Cr(NO_3)_3 \cdot 9H_2O$, 0.2877 g $MnCl_2 \cdot H_2O$

and 0.808 g $Fe(NO_3)_3 \cdot 9H_2O$ in methanol solvent. The mixtures were refluxed for half an hour only; the colored precipitates were separated, washed with methanol and finally dried in a vacuum desiccators.

Cytotoxicity against tumor cells

The toxicity of isolated complexes as well as their original salts was tested against HCT-116, HEPG-2 and MCF-7 tumor cell lines by sulfo-rhodamine B (SRB). Cells were preserved in RPMI media accomplished with 100 μg mL^{-1} streptomycin, 100 units mL^{-1} penicillin and 10% heat-inactivated fetal bovine serum in a humidified, 5% (v/v) CO_2 atmosphere at 37 °C, and the cells were sub-cultured two times in a week. Reduplicated growing cells were collected using 0.25% trypsin–EDTA and plated in 96-well plates at 1000 cells/well. Cells were exposed to the extracts for 72 h and subsequently fixed with TCA (10%) for 1 h at 4 °C. Cells were exposed, after many washing, to 0.4% SRB solution for 10 min in dark place and then washed with 1% glacial acetic acid. Tris–HCl was used to dissolve the SRB-stained cells after drying over night, and the intensity of color was determined at 540 nm. The cell viability was measured by Trypan blue (0.4) stain, permitting us to distinguish viable (non-stained) and dead (stained) cells from each other. Viable and dead cells were counted with Nikon microscope with the assistance of hemocytometer. Viable cell percentage = [1.00 − (blue cells number ÷ total cells number)] × 100. The statistical analysis was accomplished through the use of Sigma Plot version 12.0

Equipments

At micro-analytical unit, carbon, H and N were analyzed. The content of metal and the conjugated anions were determined using standard methods [15]. The molar conductivity of freshly prepared 1.0×10^{-3} mol cm^{-3} was measured for the complexes (in DMSO) using Jenway 4010 conductivity meter. The infrared spectra, as KBr disks, were obtained on JASCO FT-IR-4100 spectrophotometer (400–4000 cm^{-1}). The electronic spectra were recorded on UV$_2$ Unicam UV/Vis spectrophotometer. The effective magnetic moments were evaluated at room temperature by using a Johnson Matthey magnetic susceptibility balance. Thermal analysis was carried out on a Shimadzu thermogravimetric analyzer at a heating rate of 10 °C min^{-1} (20–1000 °C) under nitrogen. X-ray diffraction patterns (XRD) were conducted on Rigaku diffractometer using Cu/Kα radiation. Scanning electron microscopy (SEM) images were taken in Joel JSM-6390 equipment. ESR spectra of powdered complexes were recorded on a Bruker EMX spectrometer working in the X-band (9.60 GHz) with 100-kHz modulation frequency.

The microwave power was set at 1 mW, and modulation amplitude was set at 4 Gauss. The low field signal was obtained after 4 scans with a 10-fold increase in the receiver gain. A powder spectrum was obtained in a 2-mm quartz capillary at room temperature.

Theoretical calculations

Molecular modeling

Implementing Gaussian 09 software [16], the geometry of ATA compound and related VO(II), Cr(III) and Mn(II) complexes are fully optimized by Hartree–Fock exchange with LANL2DZ base set which display a good performance with transition metal systems [17–19], while the optimized geometry of Fe(III) complex was achieved employing DFT/B3LYP (3-21G base set) [9]. Gaussian output files were visualized by means of Gauss-View molecular visualization program [20]. According to the viewed numbering scheme, frontier energies (HOMO and LUMO) in gas phase are used to calculate some essential quantum parameters. Also, the charges of donor sites are abstracted from data log files for optimized structures.

Molecular docking

The simulative antitumor activity was achieved using Autodock tools 4.2 for molecular docking guest–-host complexation. Docking calculations implemented after the addition of Gasteiger partial charges to acidic drug atoms. Hydrogen atoms (non-polar) were conjoined and rotatable bonds were illustrated. The computations were performed on the ligand–protein complex. Autodock tools were achieved after the addition of; fundamental hydrogen atoms, Kollman united atom type charges and salvation parameters [21]. Affinity (grid) maps of xx Å grid points and 0.375 Å spacing were assigned applying Autogrid program [22]. Van der Waals and the electrostatic terms were computed using Auto Dock parameter set- and distance-dependent dielectric functions, respectively. Docking simulations were executed using the Solis & Wets local search method and the Lamarckian genetic algorithm (LGA) [23]. Initial position, orientation and torsions of the ligand molecules were set incidentally. All rotatable torsions were released during docking. Each docking experiment was derived from 10 different runs that were set to close after a maximum of 250,000 energy assessments. The population size was set to 150. During the search, a translational step of 0.2 Å, and quaternion and torsion steps of 5 were applied.

Results and discussion

General features

Essential physical and analytical characters for the acid ligand and its complexes are presented in Table 1. The chelate compounds are generally stable in air, having high melting points, insoluble in known organic solvents except DMSO and DMF that are completely soluble. 1:1 (M/L) molar ratio is the only formula suggested although the use of enriched multi-central ligand. This unexpected ratio may refer to the tendency of carboxylic group to the covalent attachment versus the coordination. The molar conductivities of 1 mmol L^{-1} complexes in DMSO represent 5.93–14.12 $O^{-1} cm^2 mol^{-1}$ values except Cr(III) one displays 45 $O^{-1} cm^2 mol^{-1}$. This outcome introduces their non-conducting features except Cr(III) one [24]. This feature is attributing to the covalent ability of conjugated anions (NO_3^-, SO_4^{-2} and Cl^-). However, attaching one anionic nitrate group with Cr(III) complex is reflecting the same chance for the two attachments.

Infrared investigation

Significant vibration bands of the acid and its complexes are listed in Table 2. The acid spectrum displays the following bands: 3389, 1397, 1660, 1037, 1760 and 1820 cm^{-1} attributed to υOH, δOH, $\upsilon C=O$, $\upsilon C–O$ and $\upsilon C=O(COOH)$, respectively [25]. The optimized and occupied structures of the acid ligand (Fig. 1) are

Table 1 Analytical and physical data of ATA (H_5L) ligand and its metal complexes

Compound Empirical formula (Calcd)	Color	Elemental analysis (%) Calcd/found				
		C	H	Cl or SO_4	N	M
1. [VO(SO_4)($C_{22}H_{14}O_9$)]2(H_2O)(621.37)	Reddish violet	42.53/42.49	2.92/2.92	15.46/15.54	–	8.20/8.18
2. [Cr(NO_3)$_2$($C_{22}H_{14}O_9$)](NO_3)(660.35)	Violet	40.02/40.11	2.14/2.15	–	6.36/6.36	7.87/7.88
3. [Mn(Cl)$_2$($C_{22}H_{14}O_9$)(H_2O)$_2$](H_2O)(602.23)	Greenish red	43.88/43.85	3.35/3.40	11.77/11.80	–	9.12/9.15
4. [Fe(NO_3)$_3$($C_{22}H_{14}O_9$)]2(H_2O)(718.24)	Reddish violet	36.79/36.81	2.81/2.79	–	5.85/5.84	7.77/7.75

Table 2 Significant IR spectral bands (cm^{-1}) of ATA ligand and its metal complexes

Compound	v_{OH}	δ_{OH}	$v_{C=O}$	$v_{C=O\ (COOH)}$	$v_{as}(NO_3)$, $v_s(NO_3)$	$v_{as}(SO_4)$, $v_s(SO_4)$	v_{C-O}	v_{M-O}	$\delta r(H_2O)$, $\delta w(H_2O)$
1. $[C_{22}H_{14}O_9]$	3389	1397	1660	1760, 1820	–	–	1037	–	–
2. $[VO(SO_4)(C_{22}H_{14}O_9)]2(H_2O)$	3416	1397	1549	1730, 1830	–	1332, 1219	1039	580, 650	803, 669
3. $[Cr(NO_3)_2(C_{22}H_{14}O_9)](NO_3)$	3797	1397	1557	1720, 1816	1407, 1364	–	1036	592, 670	–
4. $[Mn(Cl)_2(C_{22}H_{14}O_9)(H_2O)_2](H_2O)$	3385	1393	1560	1725, 1818	–	–	1040	580	842, 668
5. $[Fe(NO_3)_3(C_{22}H_{14}O_9)]2(H_2O)$	3382	1384	1563	1626, 1830	1470, 1320	–	1040	538, 626	834, 626
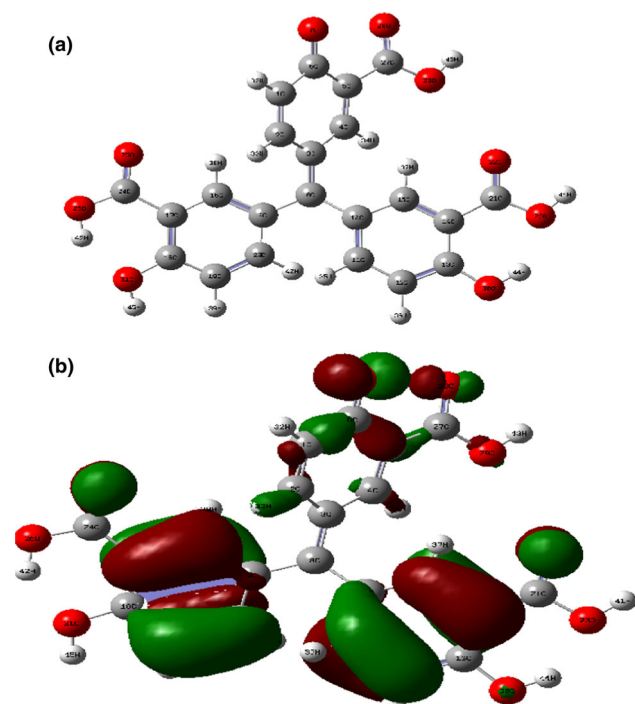
Fig. 1 Optimized and occupied structures for aurintricarboxylic acid (ATA) (**A** and **B**, respectively)

concluded to establish view for coordination mode approach accompanying with IR data.

Deliberate comparison for IR spectra is accomplished to set the basis of mode of coordination toward each metal atom. The multi-donor sites appeared with COOH, OH and C=O groups sometimes may cause obstacles prohibit assert at coordination mode. The $\upsilon C=O$ (COOH$_s$) displays lower shifted vibration around 1730 cm^{-1} beside more or less un-shift for other one (≈ 1820 cm^{-1}). This may propose the coordination of only one carbonyl in-between three groups appeared at ≈ 1820 cm^{-1}. Also, an observable lower shifted appearance for $\upsilon C=O$ group mentions its contribution in coordination. Also, this is verified by the shining of new band assigned for $\upsilon M-O$ vibration. The absence of significant lower shift for OH vibration bands mentions its ruling out from coordination. However, proposing for

water molecules attached with most complexes was mentioned superficially through the broadness centered at ≈ 3400 cm^{-1} which guides for crystal or coordinating molecules. The new bands attributed to $\delta r(H_2O)$ and $\delta w(H_2O)$ vibrations as well as TG analysis are the intensive evidences. The $[VO(SO_4)(C_{22}H_{14}O_9)]2(H_2O)$ spectrum represents especial bands (1332 and 1219 cm^{-1}) attributed to $v_{as}(SO_4)$ and $v_s(SO_4)$, respectively. The $\Delta = v_{as} - v_s$ of ~ 110 cm^{-1} are indicative for a bi-dentate bridging mode. Also, a new band at 971 cm^{-1} assigns to $v(V=O)$ specific for square-pyramidal configurations [26]. The $[Cr(NO_3)_2(C_{22}H_{14}O_9)](NO_3)$ and $[Fe(NO_3)_3(C_{22}H_{14}O_9)]$ 2(H$_2$O) spectra show bands attributed to $v_{as}(NO_3)$ and $v_s(NO_3)$ in its bi-dentate and mono-dentate features [27], respectively. Moreover, Cr(III) complex spectrum showed another band at 1330 cm^{-1} assigned for anionic nitrate group attached.

Electronic transitions and magnetic features

In DMSO solvent, significant electronic spectral bands were deducted as well as the magnetic susceptibility values are presented in Table 3. The free-acid spectrum shows bands at 33,695, 26,318, 19,660 and 16,666 cm^{-1} attributed to several $\pi \rightarrow \pi^*$ and $n \rightarrow \pi^*$ intra-ligand transitions. The acid deep color may refer to the high conjugation for chromophore groups in the ligand configuration. This affects the position of CT bands which is nearby visible range and deepens the color of the compound. The spectrum of $[VO(SO_4)(C_{22}H_{14}O_9)]2(H_2O)$ complex exhibits three d–d transition bands at 20,408, 19,231 and 12,280 cm^{-1} assigned for $^2B_{2g} \rightarrow ^2A_{1g}(v_3)$, $^2B_{2g} \rightarrow ^2B_{1g}(v_2)$ and $^2B_{2g} \rightarrow ^2Eg(v_1)$, respectively, in square-pyramidal configuration (Fig. 2A). The magnetic susceptibility value (1.77 BM) falls in the normal rang for d^1 systems. The spectrum of $[Cr(NO_3)_2(C_{22}H_{14}O_9)](NO_3)$ exhibits significant internal d-transition bands at 22,845 and 16,870 cm^{-1} attributing to $^4A_{2g}(F) \rightarrow ^4T_{1g}(F)$ (v_2) and $^4A_{2g} \rightarrow ^4T_{2g}(F)$ (v_1), respectively, in octahedral configuration (Fig. 2B). The magnetic susceptibility value

Table 3 Magnetic moments (BM) and electronic spectra bands (cm^{-1}) of the investigated compounds

Comp.	μ_{eff}/BM	d–d transition/cm^{-1}	Intra-ligand and charge transfer/cm^{-1}	Ligand field parameters			
				Dq/cm^{-1}	B/cm^{-1}	β	Z
1.	–	–	33,695/26,318/19,660/16,666	–	–	–	–
2.	1.77	20,408/19,231/12,280	33,860/26,540	–	–	–	–
3.	3.90	22,845/16,870	34,223/28,450	1687	577.03	0.628	+1.165
4.	5.92	25,000/21,739/15,384	33,910/26,467	705.1	641	0.745	+0.958
5.	5.87	28,794/23,587/16,920	33,896/26,646	775.9	705.37	0.820	+1.217
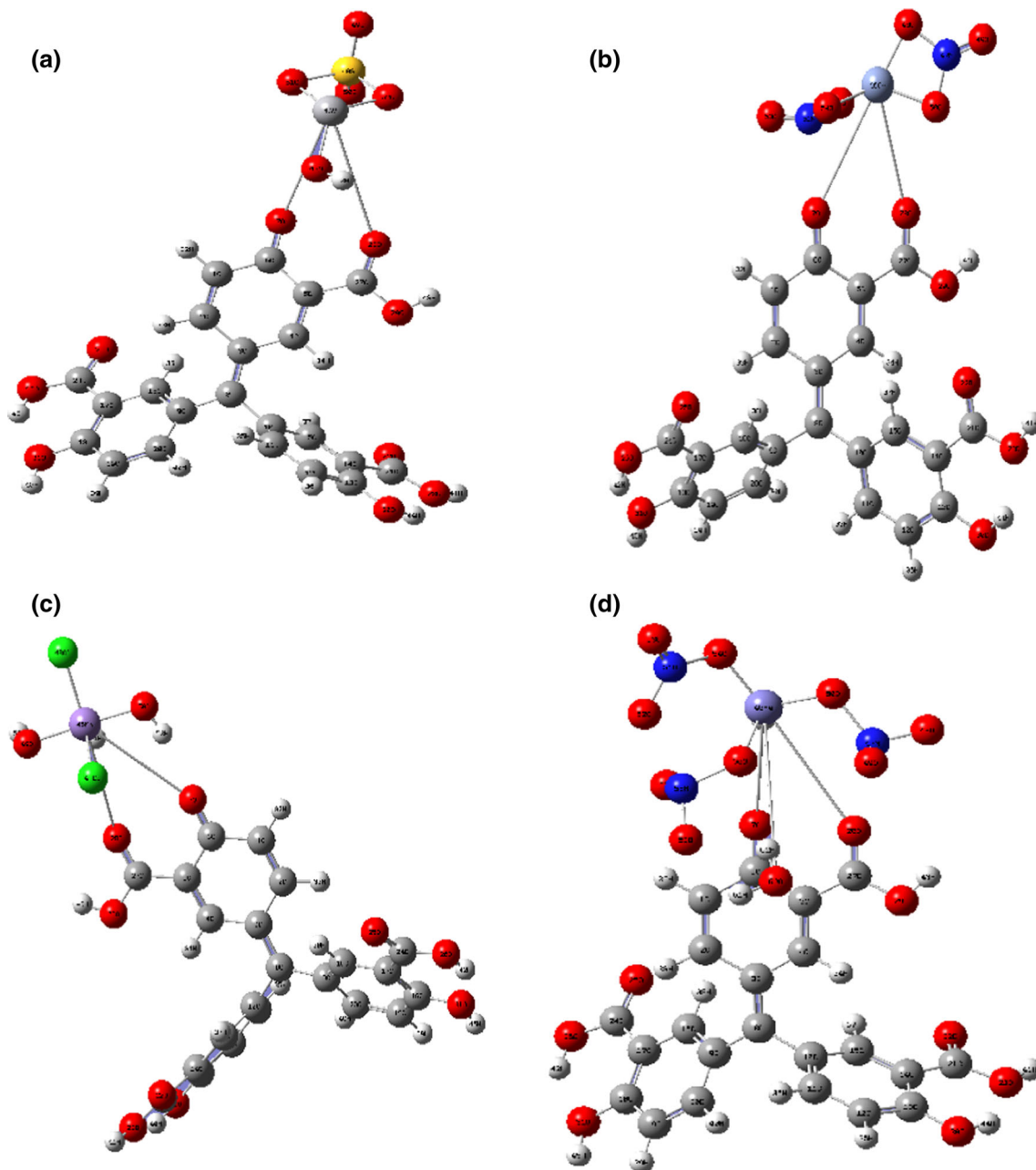
Fig. 2 Optimized structures for VO(II), Cr(III), Mn(II) and Fe(III)-ATA complexes (**A**, **B**, **C** and **D**, respectively)

(3.90 BM) agrees with spin-only moment. The Racah parameter B value (577.03 cm^{-1}) was calculated using standard equation [28]. β parameter which is called nephelauxetic parameter is obtained using: $\beta = B$(complex)/B^o(free ion) relation. The β value (0.628) obtained from considering for low-energy quartet-doublet transitions is reflecting a strong covalence of metal–ligand σ bonds which agrees with Cr–O bonds [29]. The $[Mn(Cl)_2(C_{22}H_{14}O_9)(H_2O)_2](H_2O)$ spectrum exhibits three d–d transition bands at 25,000, 21,739 and 15,384 cm^{-1}. These bands are attributing to $^6A_1g \rightarrow {}^4$Eg, $^4A_1g(G,v_3)$, $^6A_1g \rightarrow {}^4T_2g$ (G,v_2) and $^6A_1g \rightarrow {}^4T_1g(G, v_1)$ transitions, respectively, in octahedral configuration (Fig. 2C). The magnetic susceptibility value (5.92 BM) agrees with spin-only moment expected with high-spin low-field d^5 complexes. The Dq, Racah and nephelauxetic parameters values (705.1 cm^{-1}, 641 cm^{-1} and 0.745) were calculated, displaying the relative shift from elemental shape and a considerable covalent attachment for Mn–O. The $[Fe(NO_3)_3(C_{22}H_{14}O_9)]$ 2(H_2O) spectrum exhibits feature nearby the Mn(II) complex suitable for d^5 systems. The magnetic susceptibility value (5.87 BM) agrees with the high-spin octahedral complexes (Fig. 2D). The Dq, Racah and nephelauxetic parameters values (775.9 cm^{-1}, 705.37 cm^{-1} and 0.82) were calculated. The nephelauxetic parameter reflects the relative ionic attachment of Fe–O bonds. The Racah inter-electronic repulsion parameter values are varied for $3d$ transition metal complexes with changing Z and q values, where Z is the charge of cation effectively found and q is the number occupied by d- shell as d^q. The Racah parameter is expressed as follows:

$$B\left(cm^{-1}\right) = 384 + 58q + 124(z+1) - 540/(z+1) \quad (1)$$

The effective metal charges are +1.16, +0.95 and +1.21 for Cr(II), Mn(II) and Fe(III) ions, respectively. These accounts are considerably below than the formal charge of the ions. This reduction in oxidation state is suitable for M–O bond with high charge transfer [30, 31].

EPR investigation

The EPR study concerning VO(II), Cr(III) and Mn(II) complexes was achieved. This study puts a wide view over the structural geometry proposed for paramagnetic complexes. The spin Hamiltonian parameters deducted from powdered spectra are given in Table 4 with some MO parameters computed based on experimental data. The EPR spectrum of VO(II) complex executed at room temperature (Fig. 3A) displays eight-line manner conformable to the regular parallel and perpendicular compositions of g factor and hyperfine (hf) A-tensors. The splitting lines in the spectrum reveal that the components are well determined. Super-hyperfine splitting is not appeared, which points to

the location of unpaired electron in d_{xy} orbital [32]. The modality submits that the g and A parameters are axially symmetric in nature. The parameters are in agreement with the values commonly observed for square-pyramidal geometry of vanadyl complexes [33]. According to Hathaway [34, 35], the greater the G value (4.496) than 4, the negligible exchange interaction between metal centers supports the mono-nuclear manner. The coefficient of molecular orbital, α^2 and β^2, was calculated using known equations [36]. Hyperfine coupling constants are negative, so the calculations were performed taking A_{11} and $A_\perp$ as negative values to give positive values for β^2 and α^2 MO. In this study, α^2 (0.568) is less than β^2 (0.933) points to the in-plane σ-bonding which is more covalent than in-plane π-bonding. The Uv/Vis spectrum shows two bands at 12,280 (v_1) and 19,231 cm^{-1}(v_2) assigned to $^2B_2g \rightarrow {}^2$Eg and $^2B_2g \rightarrow {}^2B_1g$ transitions, respectively. Using first- and second-order perturbation theory, simulating pure d-orbitals was resolved. The spin Hamiltonian parameters correlating to the transition energies are expressed by:

$$g_{||} = g_e - (8\lambda/v_2) \quad \text{and} \quad g_\perp = g_e - (2\lambda/v_1) \quad (2)$$

where g_e is the free-electron value (2.0023). Using the transition values (v_1 and v_2), the spin orbital coupling constant (λ) (154.57 cm^{-1}) is evaluated. The λ value reported for free V(IV) ion is 250 cm^{-1}[36]. The reduction of λ magnitude may be due to double-bonded oxovanadium complex attributed to substantial π-bonding, in which the value is within the reasonable limits for predicated values.

Calculation of dipolar term (p)

The p value is calculated from the following equation:

$$p = \frac{7(A_{11} - A_\perp)}{6 + 3/2\,(\lambda/\Delta E_1)} \quad (3)$$

If A_{11} is taken to be negative and $A_\perp$ positive, the p value will be more than 270 G, which is far from the expected value. Thus, the signs of both A_{11} and $A_\perp$ are taken as negative and are indicated in the form of isotropic hf constant (A_o). McGarvey calculated the p value to be +136 G for vanadyl complexes [37], and the value calculated for the investigated complex (110.61 G) do not deviate much.

Calculation of MO coefficients and bonding parameters

The g-values calculated are generally so far from g_e (2.0023) for vanadyl complexes. This lowering is related to spin orbit interaction of d_{xy} ground-state level with low-lying excited states. The isotropic and anisotropic (g_o and A_o) parameters are calculated from the following equation.

Table 4 Spin—hamiltonian parameters of VO(II), Cr(III) and Mn(II) complexes(A and $p \times 10^4$)

Complex	g_{11}	$g_\perp$	g_o	A_{11}	f	$A_\perp$	A_o	p	k	G	γ	α^2	β^2
2.	1.938	1.988	1.971	165	117.45	70	101.67	110.61	0.888	4.496	0.618	0.568	0.933
3.	1.982	1.960	1.967	–	–	–	–	–	–	0.480	0.465	–	–
4.	–	–	1.977	–	–	–	–	–	–	–	–	–	–

Fig. 3 ESR spectra of VO(II), Cr(III) and Mn(II) complexes, **A**, **B**, **C**, respectively
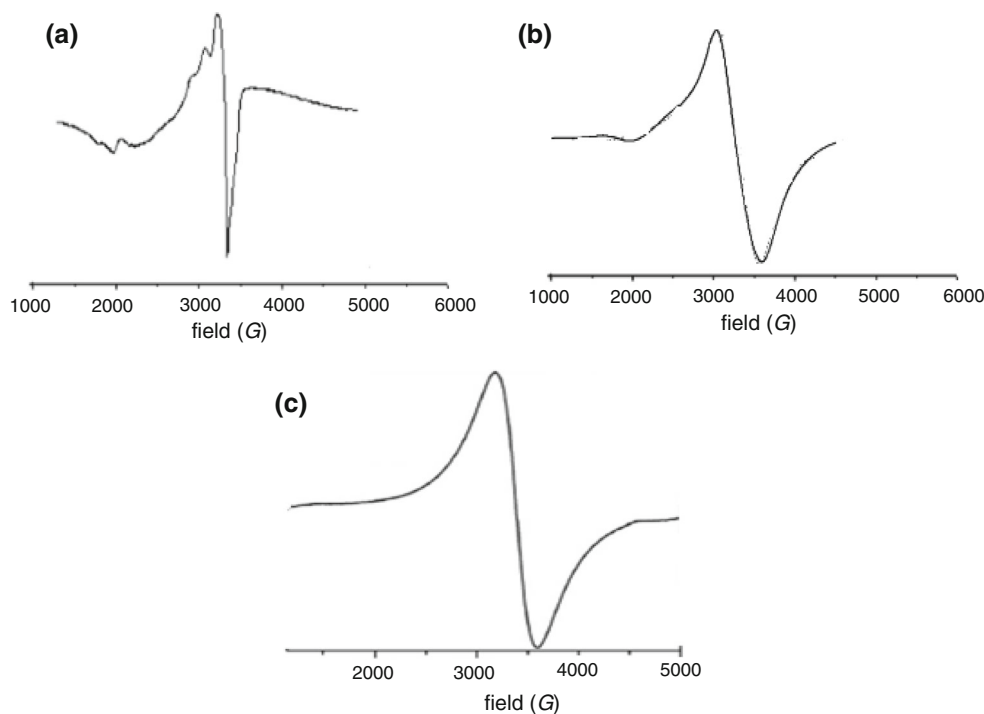
$$A_o = (A_{//} + 2A_\perp)/3 \quad \text{and} \quad g_o = (g_{//} + 2g_\perp)/3 \qquad (4)$$

The K value (fermi contact term) can be evaluated (0.84) applying known expression [38] after using anisotropic by negative values.

The powdered EPR spectrum of Cr(III) complex (Fig. 3B) represents data verified the octahedral configuration. Using this expression, $g = 2.0023(1 - 4\lambda/10 \text{ Dq})$, the g-values are calculated by, where λ is the spin–orbit coupling constant for the metal ion [39, 40]. Owen [41] calculates the reduction in spin–orbit coupling (λ') from the free-ion value ($\lambda = 90 \text{ cm}^{-1}$) for chromium(III). This is employed for measuring metal–ligand covalence. The $\lambda'(42.8)$ value indicates that the complexes under study have substantial covalent character. Six coordinated geometries are proposed based on g-values (1.982 and 1.960). It is possible to define covalence parameter ($\gamma = \lambda'/\lambda$) analogous to nephelauxetic parameter, which is the ratio for spin–orbit coupling constant of the complex to the free chromium(III) ions.

The EPR spectrum of Mn(II) complex is shown in Fig. 3C. The spectrum exhibits a broad signal centered at $g_{av} = 1.977$ regular for the fine structure of $S = 5$ spin state of Mn(II). This is similar to those reported for octahedral geometry. The broadening in EPR signals is obtained from the resonances between Mn(II) ions in crystal lattice, which collapse to a single line.

X-ray diffraction

The XRD patterns were executed at $10° < 2\theta < 90°$ range for the acid and its complexes [Fig. 4, 1S] to give an insight about the lattice dynamics of solid compounds. The clear patterns reflect the exclusion for contamination from starting materials. Known methods [42] were used to emphasize the obscurity of peaks attributed to the reactants. The Cr(III) and Mn(II) complexes beside their original acid patterns reflect their nano-crystalline features [43, 44], while VO(II) and Fe(III) complexes introduce

(a)

(b)
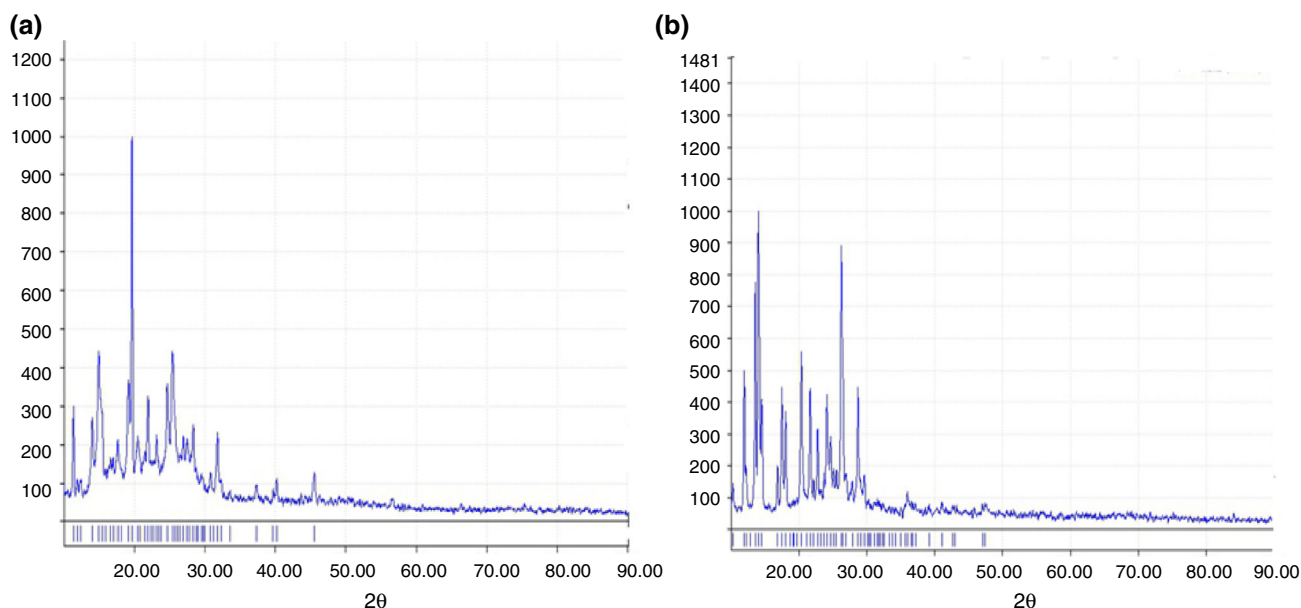
Fig. 4 X-ray manners of the acid and Cr(III) complex, **A** and **B**, respectively

Table 5 XRD spectral data of ATA (H₅L) ligand and its nano-crystalline complexes

Compound	Size/nm	θ	Intensity	d-spacing/Å	FWHM
ATA	8.461	9.825	1466.32	4.514	0.1737
Cr(III)-ATA	5.658	7.025	1481.73	6.297	0.2579
Mn(II)-ATA	9.497	20.02	1977.25	2.2503	0.1623

their amorphous nature. This may be coherent with their isolation in a fast reaction which may yield amorphous products. The θ, d values, full width at half maximum (FWHM) of prominent intensity peak, relative intensity (%) and particle size of crystalline compounds were tabulated (Table 5). Applying FWHM for characteristic peaks using Deby–Scherrer equation:

$$B = 0.94\lambda/(S \cos \theta) \tag{5}$$

The crystallite size was calculated, where S is the crystallite size, θ is the diffraction angle, B is the line width at half maximum height and Cu/Kα (λ) = 1.5406 Å. The inner crystal plane d-spacing values were determined by using Bragg equation: $n\lambda = 2d\sin(\theta)$ at $n = 1$. The range of sizes calculated (2–6 nm) is efficiently located in nanometer range.

Scanning electron microscopy

SEM images of samples are not well resolved, because samples are highly magnetic, and intensity of electron beam of SEM may not sufficient to provide the required resolution to estimate the particle size. Thus, the particles are not well resolved so will be magnified. This fact makes it impossible to make accurate estimation for distributed particles in SEM images of samples. The analysis here was carried out to check the surface morphology of the acid ligand and its complexes. The micrographs of acid ligand and its VO(II), Cr(III), Mn(II) and Fe(III) complexes are investigated (Fig. 2S). The micrographs indicated that the presence of well-defined crystals is free from any shadow for metal ions on their external surface morphology. From SEM study, the synthesized metal complex crystals were found to grow up from a single molecule to several molecules in an aggregate distribution with particle sizes starting from a few nanometers to several hundred. Moreover, different morphological shapes of metal-ATA complexes were deducted and these images were quite different from that of free acid. The difference in metal complex shapes may attribute to crystal aggregates deposited on the thin films mainly depends on the metal ions. On the other hand, it can be seen a rock-like appearance with numerous territorial patches are generally observed. In agreement with XRD patterns, the feature of VO(II) and Fe(III) complexes may reflect their amorphous nature with a complicated interpretation due to unclear appearance. Estimated size ranges are found to be: 0.52–5.68, 0.25–1.42 and 2.2–25.3 μm for acid ligand, Cr(III) and Mn(II) complexes, respectively. The observed particle diameters are out of nano-scale range which may reflect the inexact determination for such magnetically features. This appearance may affect the magnetic characters of investigated complexes.

Thermal analysis

Assuming behavior for thermo-gravimetric analysis was translated to more adaptable data (Table 6). The acid ligand displays four successive degradation stages along the process starting at 20 °C to 800 °C. The degradation process may be attributed to the removal of branches as $CO_2 + H_2O$ gases and followed by the degradation of C_7H_3 moiety in the second step. The final two follower steps may attribute to complete degradation for the organic compound till 800 °C with carbon atoms residue. The residual carbons proposed due to the process was carried out under nitrogen in the absence of environmental oxygen for complete vaporization. The investigated complexes display lower thermal stability except Cr(III) one. This reduced stability is attributed to hydrated water molecules inconvenient with IR investigation. Three to four degradation stages are the general feature with all complexes till reaching ≈ 700–750 °C. VO(II) and Cr(III) complexes starting their degradation at 25 and 110 °C, respectively, assign to the removal of outer coordination sphere molecules beside a part from organic acid. The following three steps ended at ≈ 700 °C represent complete degradation for the coordinating system. The residue is compatible with $VOSO_4$ or polluted CrO_3. Mn(II) and Fe(III) complexes

starting their degradation at ≈ 25 °C assign for the removal of water molecules in crystal or coordinating feature. The following two steps ended at 680 and 750 °C, respectively, represent the complete degradation for the coordinating system. The residue is compatible with MnO or polluted FeO. The high conformity between the calculated and found mass loss in the degradation stages reflects the absence of overlapping between the following stages and the exact determination for the stages boundaries (examples Fig. 3S).

Theoretical investigation

Computational Molecular modeling

Gaussian 09 program is used to optimize the structures for free acid and its metal ion complexes (Fig. 2). Also, to deduce important quantum parameters intense and verify the coordination study. The frontier orbital energies (E_{HOMO} & E_{LUMO}) were calculated for viewer optimized structures and the energy gap ($E_H - E_L$) used to deduce different parameters which clarify their comparative capacities [45]. The free-acid MO images (Fig. 4S) display that the HOMO and LUMO levels are centered in C=C groups of 6-membered rings with excluding for donor

Table 6 Thermogravimetric analysis data for investigated compounds

Complex	Steps	Temp. range/°C	Decomposed	Mass loss; found (Calcd. %)
1.	1st	20–200	$-CO_2 + H_2O$	14.68/14.66
	2nd	200–400	$-C_7H_3$	20.62/20.61
	3rd	400–500	$-CO_2 + H_2O$	14.68/14.67
	4th	500–800	$-C_{11}H_7O_3$	44.31/44.52
	Residue		2C	5.69/5.54
2.	1st	25–200	$-2H_2O + CO_2 + H_2O$	15.78/15.78
	2nd	200–330	$-CO_2 + H_2O$	9.58/9.98
	3rd	330–530	$-2(C_6H_3) + CO_2 + 0.5H_2$	31.84/31.44
	4th	530–750	$-C_7H_3O$	16.29/16.59
	Residue		$VOSO_4$	26.21/26.23
3.	1st	110–350	$-3NO_2 + 1.5O_2 + C_7H_5O_3$	49.11/48.93
	2nd	350–420	$-CO_2 + H_2O$	9.30/9.39
	3rd	420–550	$-C_7H_3$	13.21/13.19
	4th	550–700	$-C_5H_4$	9.82/9.70
	Residue		$CrO_3 + 2C$	18.56/18.78
4.	1st	25–200	$-3H_2O + Cl_2$	20.88/20.74
	2nd	200–460	$-C_{15}H_{10}O_6 + CO_2$	54.82/54.84
	3rd	460–680	$-C_6H_4$	12.52/12.64
	Residue		MnO	11.78/11.78
5.	1st	27–200	$-3H_2O + 3NO_2 + 1.5O_2$	33.55/33.42
	2nd	200–440	$-2(C_7H_5O_3)$	38.10/38.18
	3rd	440–750	$-C_6H_4O_2$	15.11/15.05
	Residue		FeO + 2C	13.24/12.65

centers which is relatively free for coordination, while the complexes of MO images introduce that the LUMO level is centered in metal atoms and their anions except with Cr(III) complex. So, the metal atoms are considered the acceptor level for charge transfer. This supports the significant reduction in the metal charges in the coordinating systems as reported in spectral part. Electronegativity (χ), chemical potential (μ), global hardness (η), global softness (S), global electrophilicity index (ω) and the absolute softness ($\bar{\sigma}$) were evaluated according to definite equations [46, 47]. Electrophilicity index (ω) is one of the most important quantum chemical descriptors in describing toxicity and the reactivity of various selective sites. The electrophilicity may quantify the biological activity of drug receptor interaction. Also, this index measures the stabilization energy when the system acquires extra negative charge from the environment. η and $\bar{\sigma}$ indexes are the measure for molecular stability and reactivity, and also, their concepts are related to each others. The softness index is the vice verse image for global hardness [48].

Quantum parameters The data calculated and displayed in Table 7 reflect significant observations belong to free acid and its complexes. The parameters calculated belong to the free acid introduce the high energy gap attribute to the first electronic transition. The transition band appears in visible region due to the presence of multi-chromophores. The acid form has a soft character with high flexibility reflecting its reactivity. The positive electrophilicity index (χ) value and the negative electrochemical potential (μ) value indicate that the molecule capable of accepting electrons from the environment and its energy must decrease upon accepting electronic charge. Therefore, the electrochemical potential must be negative.

Quantum parameters belong to the complexes display comparable energy gap with respect to free acid except Fe(III) complex. The frontier energy gap (ΔE) may reflect relatively softness conformity in-between the acid and its VO(II), Cr(III) and Mn(II) complexes. This is reflecting the nearby biological activity except Fe(III) complex. This is the expected behavior with acid known to its inhibition activity toward DNA and RNA polymerase. The E_{HOMO}

values elevated from the free ligand may be accompanied with the elongation for metal–ligand bonds. The dipole moment values ordered by: Mn(II) > VO (II) > ATA > Cr(III) > Fe(III). This may reflect the presence of overall charge upon the complexes with the priority of ionic interaction with Mn(II) ion. This agrees considerably with the calculated effective charge for central atoms from spectral data. In agreement with spectral data, significant reduction in Cr(III) and Fe(III) charges in comparison with Mn(II) ion throws a shadow on the dipole moment arrangement.

Atomic charges

According to the numbering scheme of optimized structures (Fig. 2), the atomic charges were calculated (Table 8). The coordinating sites may be O(7) and O(29) in-between multi-intensive centers in ATA ligand. This proposal may refer to farness geometrical distribution of highly charged centers to be interact with one central atom, subsequently, a chosen sites in-between are contributing on behalf. These two sites suffering a considerable reduction in charges in comparison with the others, due to their contribution in coordination mode.

Molecular docking

Recently, the computational capacity enhanced dramatically by using more sophisticated and computationally intense methods in computer-aided drug design. The Autodock tools used to predict the biological features of candidate drug or emphasis on experimental results. This study interested in using known drug inhibits DNA polymerase and E-Coli to bind with other host cancer protein receptors. The chosen host receptors attribute to cancer types used in antitumor application used in this study for conformity. Breast cancer (1jnx), colorectal carcinoma (2hq6) and hepatic carcinoma (2jw2) are the receptors docked with ATA drug (inhibitor) in comparison with DNA polymerase(3c2 k) and E-coli (2jvu) receptors. The calculated energies for the docking process are presented in Table 9. The free energy of binding, inhibition constant,

Table 7 HF/DFT parameters calculated for ATA (H$_5$L) ligand and its complexes

Compound	E_H/eV	E_L/eV	$(E_H - E_L)$/eV	$E_L - E_H$	x/eV	μ/eV	η/eV	S/eV^{-1}	ω/eV	$\bar{\sigma}$/eV
H$_5$L	−0.27584	−0.04076	−0.2351	0.23508	0.1583	−0.1583	0.11754	0.05877	0.106597	8.507742045
VO(II)	−0.32442	−0.03628	−0.2881	0.28814	0.18035	−0.18035	0.14407	0.072035	0.112883	6.941070313
Cr(III)	−0.33298	−0.00581	−0.3272	0.32717	0.169395	−0.1694	0.163585	0.081793	0.087706	6.113029923
Mn(II)	−0.34484	−0.11965	−0.2252	0.22519	0.232245	−0.23225	0.112595	0.056298	0.239521	8.881389049
Fe(III)	−0.23162	−0.18159	−0.05	0.05003	0.206605	−0.20661	0.025015	0.012508	0.853201	39.97601439

Table 8 Significant atomic charges and dipole moment/Debye of ATA ligand and its complexes

	O^7	O^{22}	O^{23}	O^{25}	O^{26}	O^{28}	O^{29}	O^{30}	O^{31}	Dipole moment
1.	−0.347349	−0.420572	−0.187171	−0.409759	−0.099239	−0.386746	−0.157565	−0.116388	−0.220624	17.6542
2.	−0.322946	−0.429448	−0.187713	−0.411366	−0.100638	−0.400878	−0.156734	−0.126062	−0.225348	22.7022
3.	−0.330730	−0.429291	−0.187844	−0.411170	−0.101459	−0.396293	−0.155791	−0.120773	−0.227964	16.4864
4.	−0.337676	−0.428244	−0.186246	−0.411561	−0.097866	−0.434300	−0.148831	−0.121969	−0.222485	23.7884
5.	−0.332381	−0.483361	−0.216318	−0.474210	−0.205429	−0.500701	−0.155686	−0.239973	−0.247481	11.4376

Table 9 Molecular docking energy values obtained for ATA ligand toward different receptors

| Receptor	Est. free energy of binding/kCal/mol	Est. inhibition constant (K_i)/uM	vdW + bond + dissolve energy/kCal/mol	Electrostatic Energy/kCal/mol	Total intercooled energy/kCal/mol	Frequency (%)	Interact surface
1jnx	+13.76	–	+11.18	−0.10	+11.08	10	638.644
2hq6	−4.44	557.71	−6.21	−0.09	−6.30	10	546.2
2jw2	−3.27	4.01	−4.72	+0.15	−4.57	10	644.58
3c2k	−5.71	65.40	−6.61	−0.69	−7.30	60	879.154
2jvu	−4.01	1.15	−5.69	−0.23	−5.92	20	669.053

electrostatic energy, total intercooled energy and interact surface for receptor–inhibitor complexes were deduced. So, the reduction in binding energy due to alteration will increase the inhibitor binding affinity toward protein receptors [49]. These data introduce the best interaction stability for docked complexes (Fig. 5, 5S). According to computational calculation, HB plot curves (Fig. 6, 6S) distinguish the interaction with 2hq6 receptor beside its known inhibition area of 3c2 k or 2jvu receptor. So, an expectation for its inhibition activity toward colorectal carcinoma by efficiency is nearby its known with DNA. This is referring to variable capability of multi-central groups for H-bonding interaction inside the docked complexes. A distinguished inter-hydrogen bonding was appeared with all complexes except with 1jnx receptor,

while the drug interaction toward 1jnx receptor is completely absent which introduces ineffectiveness toward breast cancer disease. 2D- plot curves (Fig. 7S) explain the mode of interaction inside the docking complex. Finally, the antitumor activity of the investigated acid ligand will be substantially anticipated except with breast carcinoma.

Antitumor activity

With the steady increase in chemical products at various levels for different purposes, for pharmaceutical, food, antibiotics, insecticide, etc., anticancer drug design and development become one of the most important fields of synthetic chemistry. Cancer defined as uncontrolled cell division also characterized by days of regulation of
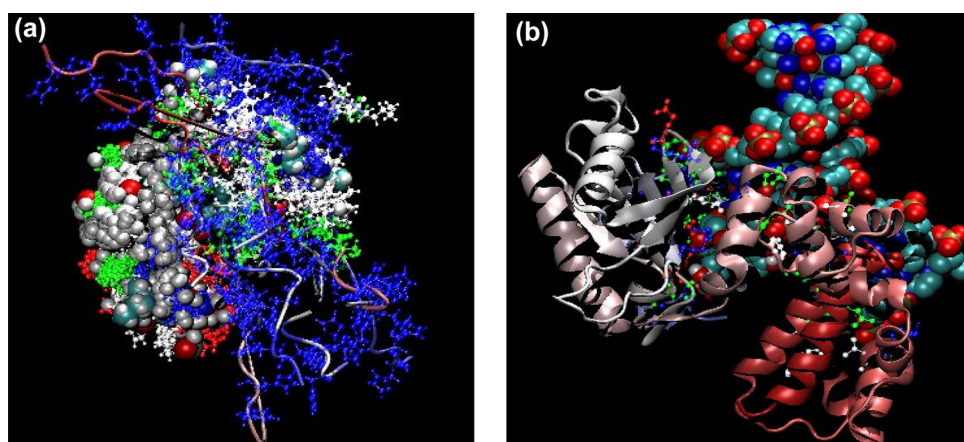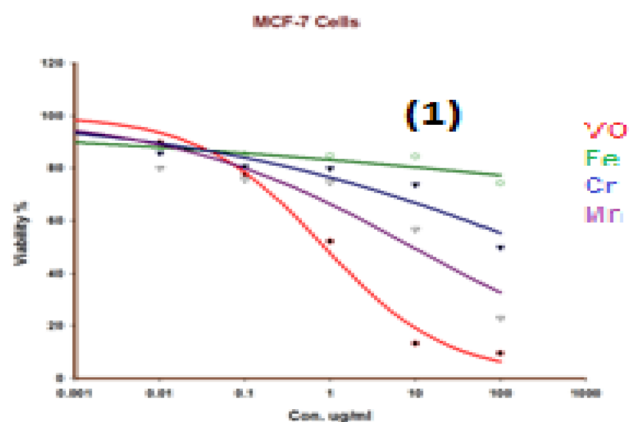

Fig. 5 Protein- inhibitor complexes for 2jw2 and 3c2k receptors (**A** and **B**, respectively)
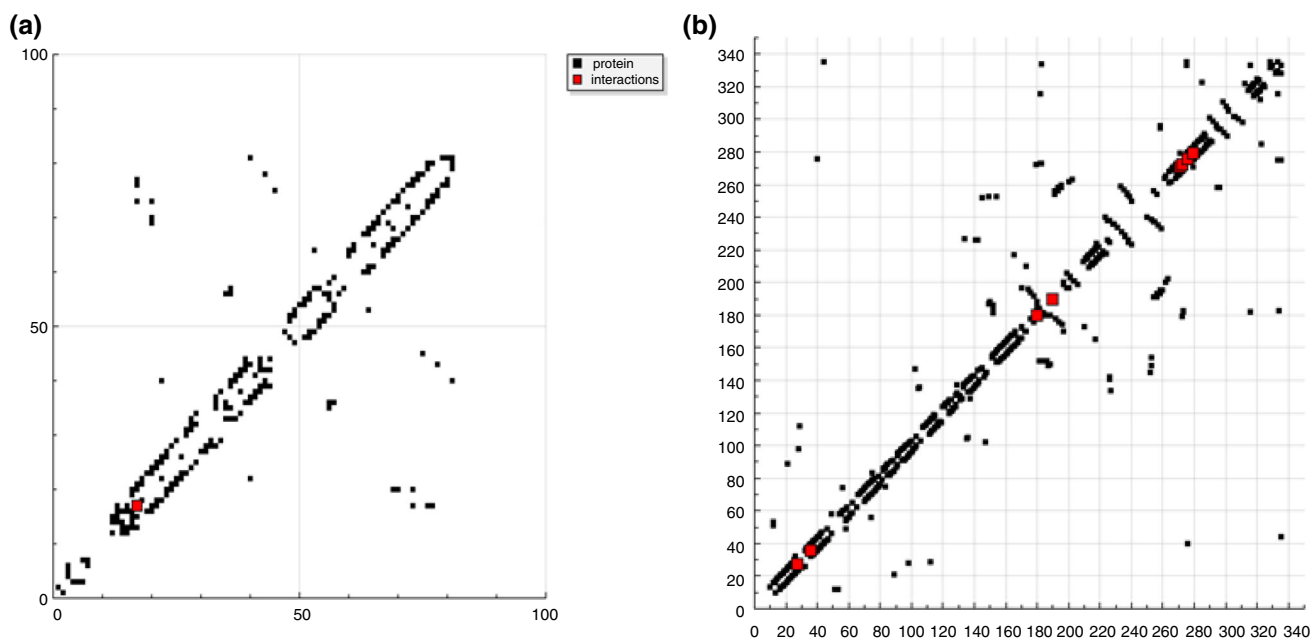
Fig. 6 HB plot of 2jw2 and 3c2k receptors with H_5L inhibitor, **A** and **B**, respectively

apoptosis, proliferation, invasion, angiogenesis and metastasis [50]. Therefore, the development of drug scan prevents or keeps one of the aforementioned cancer properties under control considered as a victory. In this study, free acid and its complexes (Fig. 7, 8S) in comparison with original salts (Fig. 9S) were comparatively investigated for their anticancer features. Mn(II) samples showed moderate activity in its complex or simple salt features (sample 4), whereas Cr(III) and Fe(III) samples were kept their insignificant effect as in complex or salt forms in all cell lines. Furthermore, the results showed that the VO(II) complex (sample 2) and salt display the major effect on different carcinoma cell lines. It is known that the vanadium metal can induce and activate different pathways inside the cell. Our study confirmed that vanadium can

induce apoptosis in different cancer cell line (HepG2, MCF-7 and HCT116) in vitro with doxorubicin data (0.777, 1.358 and 0.8105, respectively). Its low toxicity and the anticancer ability suggest vanadium as a candidate antineoplastic agent against human cancer. In the light of these results vanadium complex candidates to be used as cancer therapy. The mechanism of action may be discussed on the basis of chelation theory [51]. On chelation, the charge of metal ion will be reduced by great extent due to the overlapping with donor orbitals. Further, increases in p-electrons delocalization over the whole chelate ring may enhance the complex lipophilicity. The lipophilicity enhances the penetration of the complexes into lipid membranes and blocking the metal binding sites on the enzymes of the microorganism. Also, however, the metal salts alone exhibit a higher activity but cannot be used as inhibitor agents because of their toxicity. Also, the probability of metal binding toward biological systems is expected leading to complete blocking for active systems in the cell.

Conclusions

Novel (ATA) complexes were synthesized and well characterized. All spectral data confirm the molecular and structural formula for the complexes. Octahedral structure was proposed for all complexes except VO(II) square-pyramidal configuration. Gaussian 09 program (HF/DFT) was implemented to optimize the structural formula of the compounds as well as essential quantum parameters were

Fig. 7 Dose response curves of metal complexes against MCF-7

calculated. Molecular docking tools represent distinguished bounds toward colorectal and hepatic carcinoma cell lines. This may clarify the experimental antitumor activity results for complexes. VO(II) complex displays distinguished inhibition activity toward human carcinoma cell lines. The excellence antitumor activity result for VO(II) complex may be considered the main goal achieved in our study.

References

1. Michal H, Rachel B, Avraham K. Aurintricarboxylic acid Induces a distinct activation of the IGF-I receptor SIGNALING within MDA-231 Cells. Endocrinology. 2002;143:837.

2. KadhierA F. Spectrophotometric study and characterization of aurintricarboxylic acid as analytical reagent for manganese (II) determination. J Kerbala Univ. 2009;7:190.

3. Skidmore AF, BeebeeT J. Characterization and use of the potent ribonuclease inhibitor aurintricarboxylic acid for the isolation of RNA from animal tissues. Biochem J. 1989;263:73.

4. Delol H. Modified method for preparation of aurintricarboxylic acid and prepare of it's chromium (III) complex: study its interaction with some human serum proteins. J Kerbala Univ. 2007;5:65.

5. Willing A, Follman H, Auling G. Ribonucleotidereducyase of brevibacterium-ammoniagenes is a manganese enzyme. Eur J Biochem. 1988;170:603.

6. Triller MU, Hsieh WY, Pecoraro VL, Rompel A, Krebs B. Preparation of highly efficient manganese catalase mimics. Inorg Chem. 2002;41:5544.

7. Gasser G, Ott I, Metzler-Nolte N. Organometallic anticancer compounds. J Med Chem. 2011;54:3.

8. Mitic N, Noble CJ, Gahan LR, Hanson GR, Schenk G. Metal-ion mutagenesis: conversion of a purple acid phosphatase from sweet potato to a neutral phosphatase with the formation of an unprecedented catalytically competent $Mn^{II}Mn^{II}$ active site. J Am Chem Soc. 2009;131:8173.

9. Russo MG, Vega Hissi EG, Rizzi AC, Brondino CD, Salinas Ibañez AG, Vega AE, Silva HJ, Mercader R, Narda GE. Synthesis, physicochemical characterization, DFT calculation and biological activities of Fe(III) and Co(II)-omeprazole complexes Potential application in the *Helicobacter pylori* eradication. J Mol Struct. 2014;1061:5.

10. Süss-Fink G, Cuervo LG, Therrien B, Stoeckli-Evans H, Shulpin GB. Mono and oligonuclear vanadium complexes as catalysts for alkane oxidation: synthesis, molecular structure, and catalytic potential. Inorg Chim Acta. 2004;357:475.

11. Tracey AS, Crans DC. Vanadium Compounds. Chemistry, Biochemistry and Therapeutic Applications; ACS Symposium Series 711; ACS: Washington, D.C; 1998.

12. Thompson KH, McNeill JH. OrviC. Vanadium compounds as insulin mimics. Chem Rev. 1999;99:2561.

13. Dong Y, Narla RK, Sudbeck E, Uckun FM. Synthesis, X-ray structure, and anti-leukemic activity of oxovanadium(IV) complexes. J Inorg Biochem. 2000;78:321.

14. Du S, Feng J, Lu X, Wangab G. The syntheses and characterizations of vanadium complexes with 1,2-dihydroxyanthraquinone and the structure–effect relationship in their in vitroanticancer activities. Dalton Trans. 2013;42:9699.

15. Vogel AI. Text book of quantitative inorganic analysis. London: Longman; 1986.

16. Frisch MJ, et al. Gaussian 09. Gaussian Inc, Wallingford, CT: Revision D; 2010.

17. Schultz N, Zhao Y, Truhlar DG. Databases for transition element bonding: metal–metal bond energies and bond lengths and their use to test hybrid, hybrid meta, and meta density functionals and generalized gradient approximations. J Phys Chem A. 2005;109:4388.

18. Schultz N, Zhao Y, Truhlar DG. Density functionals for inorganometallic and organometallic chemistry. J Phys Chem A. 2005;109:11127.

19. Quintal MM, Karton A, Iron MA, Boese AD, Martin JML. Benchmark study of DFT functionals for late-transition-metal reactions. J Phys Chem A. 2006;110:709.

20. DenningtonR, Keith T, Millam J. GaussView, Version 4.1.2, SemichemInc, Shawnee Mission, KS;2007.

21. Halgren TA. Merck molecular force field. I. Basis, form, scope, parameterization, and performance of MMFF94. J Comput Chem. 1998;17:490.

22. Morris GM, Goodsell DS, Halliday RS, Huey R, Hart WE, Belew RK, Olson AJ. Automated docking using a lamarckian genetic algorithm and an empirical binding free energy function. J Comput Chem. 1998;19:1639.

23. Solis FJ, Wets RJB. Minimization by random search techniques. Math Oper Res. 1981;6:19.

24. Geary W. The use of conductivity measurements in organic solvents for the characterisation of coordination compounds. J Coord Chem Rev. 1971;7:81.

25. Nakamoto K, McCarthy PJ. Spectroscopy and structure of metal chelate compounds. New York: Wiley; 1968.

26. El-Metwally NM, El-Shazly RM, Gabr IM, El-AsmyAA. Physical and spectroscopic studies on novel vanadyl complexes of some substituted thiosemicarbazides. SpectrochimicaActa, Part A.2005;61:1113.

27. El-Metwaly NM. Spectral and biological investigation of 5-hydroxyl-3-oxopyrazoline 1-carbothiohydrazide and its transition metal complexes. Transition Met Chem. 2007;32:88.

28. Price ER, Wasson JR. Complexes with sulfur and selenium donors—X chromium(III) piperidyldithiocarbamates. J Inorg Nucl Chem. 1974;36:67.

29. Jorgensen CK. The nephelauxetic series. Prog Inorg Chem. 1962;4:73.

30. Sanderson RT. Inorganic chemistry, chapter 6. New York: Reinhold; 1967.

31. Stoklosa HJ. J Chem Educ. 1973;50:50.

32. Montgomery H, Lingafelter EC. The crystal structure of Tutton's salts. IV. Cadmium ammonium sulfate hexahydrate. Acta Cryst. 1966;20:728.

33. Carrano CJ, Nunn CM, Quan R, Bonadies JA, Pecoraro VL. Monomeric and dimericvanadium(IV) and -(V) complexes of *N*-(hydroxyalkyl)salicylideneamines: structures, magnetochemistry and reactivity. Inorg Chem. 1990;29:944.

34. Hathaway BJ, Billing DE. The electronic properties and stereochemistry of mono-nuclear complexes of the copper(II) ion. Coord Chem Rev. 1970;5:143.

35. Hathaway BJ. A new look at the stereochemistry and electronic properties of complexes of the copper(II) ion. Struct Bond (Berlin). 1984;57:55.

36. Dunn TM. Spin-orbit coupling in the first and second transition sews. Trans Faraday Soc. 1961;57:1441.

37. Mc Garvey BR. The isotropic hyperfine interaction. J Phys Chem. 1967;71:51.

38. Salagram M, Satyanarayana N, Radhakrishna S. Semi-empirical evaluation of molecular-orbital parameters, and spin—orbit, dipolar and fermi-contact terms of VO^{2+} ion in lattices. Polyhedron. 1986;5:1171.

39. AbragamA BleaneyB. Electron paramagnetic resonance of transition ions. Oxford: Oxford University Press; 1970.

40. Mabbs FE, Collison D. Electron paramagnetic resonance of transition metal compounds. Amsterdam: Elsevier; 1992.

41. Owen J. The colours and magnetic properties of hydrated iron group salts, and evidence for covalent bonding. Proc R Soc Lon A. 1955;227:183.

42. Cullity BD. Elements of X-ray diffraction. 2nd ed. Boston: Addison-Wesley Inc; 1993.

43. Fahem AA. Comparative studies of mononuclear Ni(II) and UO$_2$(II) complexes having bifunctional coordinated groups: synthesis, thermal analysis, X-ray diffraction, surface morphology studies and biological evaluation. Spectrochim Acta A. 2012;88:10.

44. Shahrjerdi A, Davarani SSH, Najafi E, Amini MM. Sonoelectrochemical synthesis of a new nano lead(II) complex with quinoline-2-carboxylic acid ligand: a precursor to produce pure phase nano-sized lead(II) oxide. Ultrason Sonochem. 2015;22:382.

45. Fleming I. Frontier orbitals and organic chemical reactions. London: Wiley; 1976.

46. Ray RK, Kauffman GR. EPR spectra and covalency of bis(amidinourea/O-alkyl-1-amidinourea)copper(II) complexes part II. Properties of the CuN$_4^{2-}$ chromophore. Inorg Chem Acta. 1990;173:207.

47. Chikate RC, Padhy SB. Transition metal quinone–thiosemicarbazone complexes 2: Magnetism, ESR and redox behavior of iron (II), iron (III), cobalt (II) and copper (II) complexes of 2-thiosemicarbazido-1,4-naphthoquinone. Polyhedron. 2005;24:1689.

48. Sagdinc S, Köksoy B, Kandemirli F, Bayari SH. Theoretical and spectroscopic studies of 5-fluoro-isatin-3-(N-benzylthiosemicarbazone) and its zinc(II) complex. J Mol Struct. 2009;917:63.

49. Tripathi SK, Muttineni R, Singh SK. Extra precision docking, free energy calculation and molecular dynamics simulation studies of CDK2 inhibitors. J Theor Biol. 2013;334:87.

50. Al-Iede MM, Karpelowsky J, Fitzgerald DA. Recurrent diaphragmatic hernia: modifiable and non-modifiable risk factors. Pediatr Pulmonol; 2015.

51. AtaiwSH Abou-HussenAA. Mono and Di-nuclear complexes of Cu(II) and Cu(I) with tetradentateschiff bases. Their biological activity and potential application. Egypt J Chem. 2003;46:685.